Chapter 2
Laguerre-Gauss Beams for Test Mass Thermal Noise Reduction

Test mass thermal noise was not a dominant noise source in the first generation of gravitational wave detectors. However, with the upgrade to second generation detectors, a factor of 10 increase in sensitivity in the whole frequency band is aimed for, and at such improved sensitivities thermal noise *is* expected to be one of the major limiting noise sources. The Brownian thermal noise in particular is expected to be of sufficient magnitude to obscure gravitational wave signals around the 100 Hz region in the advanced detectors, unless new techniques are employed to reduce the effect. This point is illustrated in the projected sensitivity of the Advanced LIGO detector, shown in Fig. 2.1. From the second generation onwards therefore, advancements in other areas of the interferometers, such as the implementation of higher laser powers, will make a limited impact in the 100 Hz region unless the thermal noise of the test masses can be reduced. Research into methods for reducing the effects of this noise source is therefore of paramount importance to the gravitational wave community.

2.1 Test Mass Thermal Noise

The total thermal noise of the test masses is commonly considered as a sum of four different sources of thermal noise in the phase of light reflected from the test mass. First of all, contributions from the coating and the substrate are dealt with separately, as a result of different approximations being appropriate for each of these two components of the test mass. For each of the coating and the substrate, the total thermal noise is considered as an incoherent sum of *Brownian* noise and *themo-optic* noise contributions.[1]

A rigorous description and analysis of Brownian noise, and thermoelastic and thermorefractive noises (the two components of thermo-optic noise), as well as thermal

[1] Previously, the thermo-optic noise had been considered as an incoherent sum of *thermoelastic* noise and *thermorefractive* noise. This view has been revised however, in light of the fact that thermoelastic and thermorefractive effects are not necessarily incoherent processes [11].

P. Fulda, *Precision Interferometry in a New Shape*, Springer Theses,
DOI: 10.1007/978-3-319-01375-6_2,

© Springer International Publishing Switzerland 2014

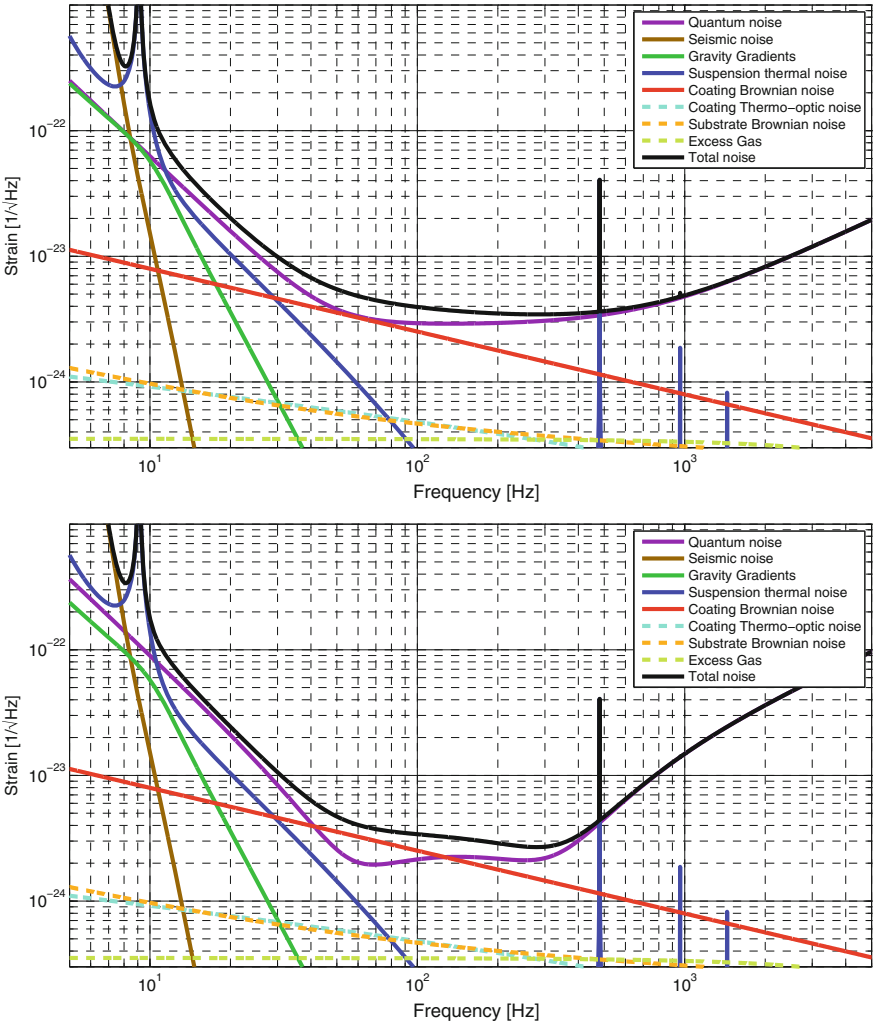

Fig. 2.1 The Advanced LIGO noise budget, in tuned signal recycling configuration for optimal broadband sensitivity (*upper plot*) and detuned signal recycling configuration for optimal sensitivity to binary neutron star sources (*lower*). The contributions of the individual noise sources are shown by the coloured lines. The quantum noise shown is the sum of shot noise and radiation pressure noise, as described in Sect. 1.5

deformation of substrates in the context of higher-order LG beams in gravitational wave detectors can be found in [31]. For a coherent treatment of thermo-optic noise for the LG_{00} mode see [11]. As yet a coherent analysis of thermo-optic noise for higher-order LG modes is not available.

2.1.1 Brownian Thermal Noise

This noise source arises due to excitations of the elastic modes of mirrors and their coatings caused by Brownian motion of their constituent atoms. These excitations lead to an uncertainty in the position of the reflecting surface. The fluctuation in the phase of the reflected light that results is indistinguishable from a phase change in the light that would be caused by gravitational waves, and thus appears as noise at the detector output. As with the suspensions, the effect of the thermal excitations can be minimised by using materials with very high Q-factors. Using high Q materials confines the fluctuations due to each resonant mode of the mirror or coating to a very narrow band around the resonance frequency. Since the resonant frequencies of the modes of oscillation lie above the observation band of the detector (>6 kHz) [24], the amplitude of oscillations within the observation band are significantly suppressed.

Brownian noise of the test mass substrates was initially calculated by summing the contributions from many normal-modes of the substrate until convergence was reached [15]. Levin showed in [24], however, that a more computationally efficient solution could be found by implementing the fluctuation dissipation theorem (FDT) [7]. Levin also showed that the FDT method calculated contributions from surface losses more accurately than the normal-mode decomposition method, which relies on the assumption of homogeneously distributed sources of friction within the material. It should be kept in mind when using the results of the FDT treatment of Levin that they also have assumptions inherent; in particular, the assumption that one is only interested in calculating the thermal noise at frequencies well below the lowest eigenfrequency of the system. While this may be a valid assumption for current designs, this should be re-evaluated for different test masses in the future, which if larger than current test masses may have resonant frequencies closer to the detection band.

Using the method described in [24], the spectral density of Brownian thermal noise is given by

$$S_x(f) = \frac{4k_B T}{\pi f}\phi\, U, \tag{2.1}$$

where T is the temperature of the relevant material, ϕ is known as the 'loss angle' and represents the retardation effect associated with dissipation in the material, and U is the strain energy at static pressure normalised for 1 N [24]. The factor U has some dependence on the material properties, but interestingly also depends on the intensity distribution of the readout beam. This is where the advantage of higher-order LG beams manifests itself, as shall be discussed in more detail later on in this chapter.

For the Brownian noise in the substrate, in the case of an infinite sized mirror where the beam radius is considered much less than the mirror radius,

$$U = \frac{1-\sigma^2}{2\sqrt{\pi} Y w}, \tag{2.2}$$

where σ is the Poisson ratio of the material, Y is the Young's modulus of the material, and w is the $1/e^2$ radius of the fundamental Gaussian mode readout beam [5]. For the Brownian noise in the coating, under the same infinite mirror approximation, Vinet showed that

$$U = \delta_C \frac{(1+\sigma)(1-2\sigma)}{\pi Y w^2} \Omega_1, \tag{2.3}$$

where δ_C is the coating thickness, and Ω_1 is a factor which includes higher order corrections due to differences between the coating material parameters and the substrate parameters [31]. It should be noted that the coating Brownian noise level, which in the second generation detectors is expected to be the leading test mass thermal noise contribution, scales with the inverse square of the readout beam size. The substrate Brownian noise level, on the other hand, scales inversely with the beam size. This dependence of the thermal noise level on beam size was the driving factor for the Advanced LIGO design to use significantly larger beam sizes on the test masses than in initial LIGO [18].

2.1.2 Thermo-Optic Noise

Thermo-optic noise arises from the fluctuating temperature field within a material. The changes in temperature couple to the phase of light reflected from the test mass in two ways; via the thermal expansion of the test mass, and the change in refractive index of the coating. Previously, these two couplings of temperature fluctuations to readout beam phase have been referred to as thermoelastic noise and thermorefractive noise respectively, as discussed in for example [25] and [6].

Thermoelastic noise is caused when the thermodynamic fluctuations cause strain fluctuations within the material as the hotter volumes expand and the colder volumes contract. These strain fluctuations then cause an additional excitation of the elastic modes of the materials, leading to uncertainties in the surface position as in the case of Brownian thermal noise. The spectral density for thermoelastic noise in the low frequency limit is given by

$$S_x(f) = \frac{k_B T}{\pi^2 f^2} W \tag{2.4}$$

where the variables are as previously defined for Brownian noise except for W, which is the average energy dissipated by the coupling of the temperature field to strain in the material [31]. This is effectively equivalent to Eq. 2.1, expect this time we consider W as the energy dissipated through coupling between the strain and the temperature field in the material. The thermal expansion coefficient α effectively determines the coupling of temperature fluctuations to strain fluctuations, and appears later in calculations of the W factor. In fused silica, α is relatively small at room temperature, and so the predicted thermoelastic noise level in gravitational wave interferometers is orders of magnitude lower than the Brownian thermal noise level.

This may not always be the case however. Sapphire has been proposed as another candidate substrate material, largely due to its good Brownian noise performance. However, the thermal expansion coefficient of sapphire is significantly higher than that of fused silica and so thermoelastic noise may be the limiting thermal noise if sapphire test masses are used in the future [28]. The choice of new substrate materials for reducing thermal noise is further discussed in Sect. 2.2.

Thermorefractive noise is similar to thermoelastic noise in that it arises from the temperature fluctuations within the material, but the coupling to phase noise is in this case via the $\frac{\partial n}{\partial T}$ coefficient; the rate of change of refractive index with temperature [11]. The level of thermorefractive noise is also expected to be orders of magnitude lower than the Brownian noise contribution for the currently used test masses, although as with thermoelastic noise, this may change in the future. Preliminary investigations have shown a very low $\frac{\partial n}{\partial T}$ coefficient for silicon at cryogenic temperatures. As is discussed in the next section, this may be an important factor in the choice of materials for the mirror substrates in future detectors.

Since these two noise sources share the same origin, however, the simple treatment of them as incoherent is not necessarily adequate. In [11], Evans demonstrates a rigorous coherent treatment of thermoelastic and thermorefractive noise, and shows that the incoherent treatment leads to an overestimation of the thermo-optic noise at 100 Hz in Advanced LIGO of around a factor of 4.

The power spectrum of the thermal fluctuations that give rise to the thermo-optic noise is given by

$$S_{TO} = \frac{2}{\pi^{\frac{3}{2}}} \frac{k_B T^2}{w^2 \sqrt{\kappa C f}}, \tag{2.5}$$

where w is the beam spot size, κ is the thermal conductivity of the material, and C is the heat capacity per unit volume of the material. Estimates for the coating thermo-optic noise level in a LIGO using this treatment put it at around a factor of 8 below the coating Brownian noise level, as shown in Fig. 2.1. As a result, Evans states that this noise source should not considered a driving force in the design of aLIGO [11]. However, this result should be re-evaluated for designs of future detectors, which may use different materials and may operate in different temperature regimes, both of which may give rise to different α and $\frac{\partial n}{\partial T}$ coefficients, as well as a different coherence level between the two dissipation processes.

2.2 Thermal Noise Reduction Techniques

2.2.1 Cryogenic Interferometry

Perhaps the most obvious technique that can be employed to reduce the level of thermal noise in gravitational wave detectors is to cool the optics and final stage

suspensions to cryogenic temperatures. The noise spectral density of *most* of the aforementioned thermal noises reduces with temperature in *most* cases, although there is the possibility for exceptions to this rule caused by the variation in α and $\frac{\partial n}{\partial T}$ with temperature.

There are unfortunately some difficulties associated with implementing cryogenic test-masses in large scale interferometers. Firstly, the test-masses are deliberately well isolated, and thus extracting heat from them is difficult. The current suspensions have a high thermal resistance due to their small cross sectional area, large length, and low thermal conductivity. Also, large low temperature baffles known as cryo-shields are required to avoid the heating up of the mirrors due to absorption of thermal radiation from the room temperature beam tubes. Cryogenic interferometry has been demonstrated nonetheless, at the Japanese interferometer CLIO [32]. A new Japanese cryogenic interferometer, KAGRA, has been funded and will begin construction very soon. This detector will serve well to elucidate the subject of cryogenic interferometry for the gravitational wave community, as well as serving as a highly sensitive detector in its own right [29].

2.2.2 New Coating Methods and Materials

The levels of all thermal noises in mirror coatings depend on the mechanical loss mechanisms of the materials from which they are made. The Q-factor of the material is of primary importance for determining how excitations caused by either the Brownian or the thermoelastic noise mechanisms translate into noise in the detector. Materials with high Q-factors confine the movement of the mirrors caused by these noise mechanisms to narrow frequency bands, and therefore mitigate the effect on the sensitivity. The level of thermo-optic noise is also determined by the α and $\frac{\partial n}{\partial T}$ coefficients, so these should be considered when choosing new materials.

Fused silica performs well enough at room temperature in all respects for the first generation of gravitational wave detectors not to be limited by thermal noise. However, the more exacting requirements of the next generation of detectors have triggered a search for better coating methods and materials, as described in for example [27] and [19]. The possibility of employing cryogenic interferometry must also be considered, as the α and $\frac{\partial n}{\partial T}$ coefficients as well as the Q-factor can vary significantly over the temperature range from a few to 300 K, in addition to the obvious gains from reducing T. Silicon has shown considerable promise as a possibly well performing substrate and coating material at low temperatures, to the extent that it is strongly considered for inclusion in the third-generation Einstein Telescope design [21].

In addition to the search for new materials, new methods of making high-reflective coatings are also being investigated. The ‘waveguide coating’ technique developed in collaboration between Jena and Hannover has shown promising results so far [14], and crystalline ‘epitaxial coatings’ are also a strong consideration in a potential Advanced LIGO upgrade [2].

2.2.3 All-Reflective Interferometers

One way to avoid the thermal problems that result from using very high laser powers is to reduce the number of transmissive optical elements that the main laser travels through. By employing diffractive grating cavities instead of the currently used transmissive ones, all reflective interferometer configurations can be designed [10]. There are two advantages of using all reflective configurations; firstly since the optics are no longer required to be transmissive, a greater selection of materials with potentially better thermal noise characteristics become viable options for substrates. Secondly in all reflective configurations less beam power will be absorbed by the optics, thus making cryogenic operation easier to achieve and reducing the impact of all thermal problems. This technology has encountered some difficulties due to the introduction of additional phase noise due to translation of the gratings [17], but on the positive side investigations into this effect were partially responsible for the development of the waveguide coating technology [14].

2.2.4 Compound End Mirrors: 'Khalili Cavities'

Another idea for reducing the effects of coating thermal noise is to employ compound mirrors in place of the end test masses [22]. The idea is based on the fact that the level of coating Brownian noise scales with the number of coating layers used to make the reflective surface of the test mass. In typical gravitational wave interferometers, most of the coating layers are on the end test mass surfaces, as these are required to have the highest reflectivity. By replacing the single end mirror with a compound mirror made up of two mirrors controlled to a state which is anti-resonant for the carrier light, a high reflectivity can potentially be achieved with significantly fewer coating layers on the first of the two mirrors. Although there will be many coating layers on the second mirror, a relatively small proportion of the light intensity will actually probe this mirror surface, and so the coupling to the detector output is small. This technology is still in early stages of development, but there are plans to test it at the Hannover 10 m prototype facility [16]. The main difficulties in employing this technique are expected to arise from the lack of geometric stability in the short cavity, and the associated problems in controlling the extra degrees of freedom that are introduced.

2.2.5 Flat Readout Beams

Spreading the readout beam power over a larger portion of the mirror surface area can reduce the thermal lensing effect and all of the substrate and coating thermal noises. This requires the introduction of so-called flat readout beams, such as higher-order

LG beams. As this technology was the main focus of the work comprising this thesis, the thermal noise advantages it may bring are described in more detail in later on in this chapter in Sect. 2.6.

2.3 The Mode Picture for Laser Beams

Throughout this thesis I will be discussing the properties of different spatial laser modes, so it is fitting to give an introduction to the concept of these modes. In this section I will first describe what is meant by the term spatial laser modes, and then describe two of the mode sets commonly used to describe the transverse properties of laser beams; the Hermite-Gauss (HG) modes and the LG modes.

The mode picture of laser beams is intimately related to the properties of light within optical resonators. In lasers, an optical resonator, or cavity, is almost always used to predefine the geometric properties and the frequency of the generated laser light. Light produced from the laser transitions in the lasing material circulates in an optical resonator, and the output beam is transmitted through a semi-transparent mirror. For the purposes of this discussion, however, we will consider a two mirror optical cavity, as shown in Fig. 2.2 with light incident on one mirror. In a similar manner to other resonators, an optical resonator has the potential to produce any of an infinite number of resonant modes. The mode of operation of a laser is defined by both the frequency of the light and the geometric properties of the beam. In the context of optical resonators, these two properties are known as the *longitudinal* and *transverse* mode orders respectively.

For the longitudinal mode order of an optical resonator, it is instructive to consider the response of an ideal optical resonator in the plane wave approximation, i.e. without considering the transverse properties of the light. The circulating power within an optical resonator for an input power of 1 W is given by

$$P_{circ} = \frac{T_1}{1 + R_1 R_2 - 2r_1 r_2 \cos(2kL)}, \tag{2.6}$$

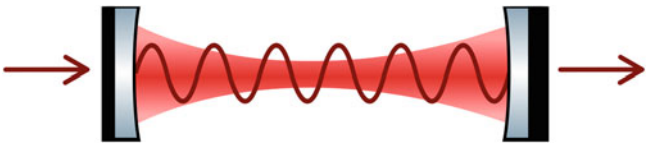

Fig. 2.2 A cartoon picture of an optical cavity. Light enters the cavity through the input mirror from the *left*, and resonates inside the cavity if its length is divisible by an integer number of half wavelengths. The maroon sinusoid represents the longitudinal mode properties, and the *red shaded area* represents the transverse mode properties

where T_1 is the power transmissivity of the input mirror, R_1 and R_2 are the power reflectivities of the input and output mirrors respectively, L is the cavity length, and $k = 2/\pi\lambda$ is the wavenumber of the light [12]. It can be seen that there is an infinite set of discrete light frequencies that give a maximal circulating light power for a given cavity length, wherever $2kL = \mathrm{n}\,\pi$ (n = 1,2,3...). This can be easily understood if we consider each resonance as a case fulfilling the criterion that an integer number of half wavelengths matches the cavity length exactly, creating a resonant standing wave inside the cavity.

The transverse mode of an optical resonator describes the geometry of the beam cross section, in a plane perpendicular to the propagation vector. An infinite set of transverse modes of an optical resonator with spherically curved mirrors can be found by solving the paraxial wave equation with the boundary conditions given by the cavity parameters, namely the cavity length and the curvatures of the mirrors. The paraxial wave equation is simply the wave equation for the electric field with the additional approximation that the light field is beam-like, i.e. varying much more rapidly along the transverse axes than the propagation axis. We can describe an electric field to be a product of a function describing the spatial properties and the oscillating function in the propagation direction z as

$$E(x, y, z) = u(x, y, z)\exp(-\mathrm{i}kz). \tag{2.7}$$

If we substitute this into the wave equation for the electric field we get

$$\frac{\partial^2 u}{\partial x^2} + \frac{\partial^2 u}{\partial y^2} + \frac{\partial^2 u}{\partial z^2} - 2\mathrm{i}k\frac{\partial u}{\partial z} = 0. \tag{2.8}$$

The condition on the variation in beam shape being slower in z than in x and y is formalised as

$$\left|\frac{\partial^2 u}{\partial z^2}\right| \ll \left|\frac{\partial^2 u}{\partial x^2}\right|, \left|\frac{\partial^2 u}{\partial y^2}\right|, \left|2k\frac{\partial u}{\partial z}\right|, \tag{2.9}$$

leading us to the paraxial form of the wave equation if we neglect the much smaller second derivative in z:

$$\frac{\partial^2 u}{\partial x^2} + \frac{\partial^2 u}{\partial y^2} - 2\mathrm{i}k\frac{\partial u}{\partial z} = 0. \tag{2.10}$$

There exist many solutions to Eq. 2.10, each representing a transverse mode of the electric field. The lowest order solution is the commonly observed Gaussian beam, with transverse field distribution given by

$$u(x, y, z) = \sqrt{\frac{2}{\pi}}\frac{1}{w(z)}\exp(\mathrm{i}\Psi(z))\exp\left(-\mathrm{i}k\frac{x^2 + y^2}{2R_C(z)} - \frac{x^2 + y^2}{w^2(z)}\right), \tag{2.11}$$

where $w(z)$ is known as the Gaussian spot size parameter,[2] $\Psi(z)$ is the Gouy phase (which is discussed in more detail in Sect. 4.3), and $R_C(z)$ is the radius of curvature of the spherical phase front.

There also exist several infinite sets of solutions to the paraxial wave equation, each including the Gaussian mode as well as higher-order solutions. The two sets which are of interest in this work are the LG modes and the Hermite-Gauss (HG) modes. Both of these mode sets are complete, which means that they can be used to construct an orthonormal basis-system in which all solutions to the paraxial wave equation can be represented as linear combinations of the basis modes. Since all beam-like electric fields should satisfy the paraxial wave equation, we can therefore use linear combinations of LG or HG modes to describe *any* beam shape.

One feature that is common to all transverse modes of spherical optical resonators is their self-reproducing intensity patterns; as they propagate, the overall scale of the transverse field distribution will change, but the shape remains constant. This is to be expected, since in order for a mode to be resonant in an optical cavity it must have the same transverse field distribution after successive round trips of the cavity. The Gaussian mode is an obvious example of a mode with a self-reproducing intensity pattern, since the propagation of a mode may be described by Fourier transforming the initial Gaussian amplitude cross section, and the Fourier transform of a Gaussian function is another Gaussian function. In the next two sections we describe the two aforementioned sets of higher-order solutions to the paraxial wave equation, the HG and LG mode sets.

2.4 The Hermite-Gauss Mode Set

The HG mode set are solutions to the paraxial wave equation in Cartesian coordinates, and exhibit rectangular symmetry. As a result of this, their amplitude profiles can be easily separated into the x and y components. The separability in x and y means that HG modes can be eigenmodes of astigmatic spherical optical resonators, which is a result of significance for the work described in Chap. 5. As a consequence of this separability, the full amplitude profile of HG modes can be expressed as

$$u_{nm}(x, y, z) = u_n(x, z)u_m(y, z). \tag{2.12}$$

The $u_n(x, z)$ and $u_m(y, z)$ functions describe the variation of amplitude in the orthogonal x, z and y, z planes, and have an identical form. The variation in the x, z plane is given by

[2] The distance from the optical axis at which the beam power is $1/e^2$ of the power at the optical axis.

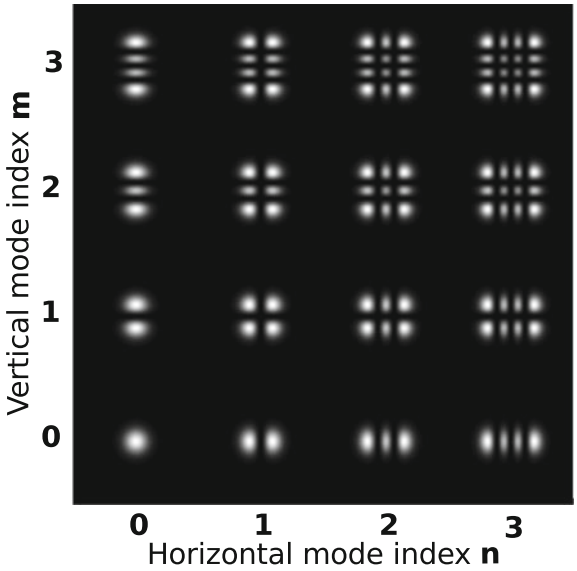

Fig. 2.3 Intensity patterns for Hermite-Gauss modes up the order 6. The intensity patterns are normalised to have the same peak intensity, for visibility

$$u_n(x,z) = \left(\frac{2}{\pi}\right)^{\frac{1}{4}} \exp\left(\mathrm{i}\,(2n+1)\,\Psi(z)\right) \times H_n\left(\frac{\sqrt{2}x}{w(z)}\right)\exp\left(-\mathrm{i}\frac{kx^2}{2R_C(z)} - \frac{x^2}{w^2(z)}\right), \tag{2.13}$$

where n is the relevant mode index, H_n is the Hermite polynomial of order n, and the rest of the parameters are as previously defined. The order of a HG mode is simply the sum of the two orthogonal transverse mode indices. The intensity patterns of the HG modes up to the order 6 are shown in Fig. 2.3.

Although we first described the higher-order HG modes as mathematical solutions to the paraxial wave equation, these modes are readily observed in a table-top optical resonator when the input beam is slightly misaligned. This is because misalignments or translations of the input beam with respect to the optical axis of the cavity cause coupling from the HG_{00} mode into higher-order HG modes. This modal description of misalignments and translations was formalised by Bayer-Helms in [3], and is illustrated in Fig. 2.4. This plot shows the amplitude cross sections of a HG_{00} mode, a HG_{10} mode, and the linear combination of both. We can see that to a reasonable approximation, the combination of the two modes appears as a translated HG_{00} mode. The addition of higher order modes to the sum, as prescribed by the Bayer-Helms relations published in [3], increases the accuracy of the description of translations in this manner. This modal description of beam shapes is employed in the interferometer

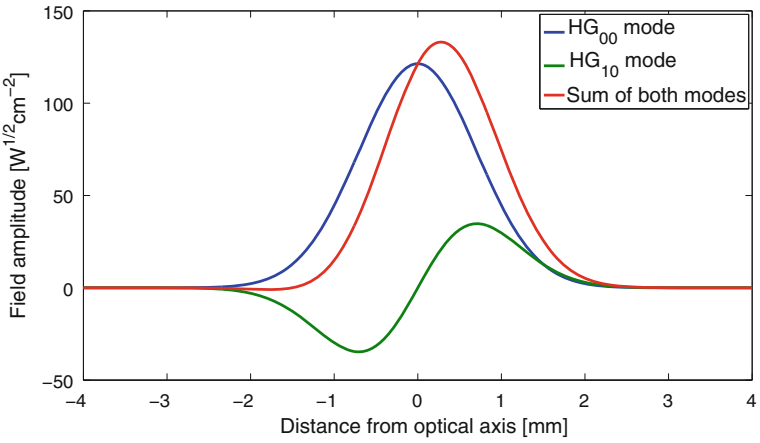

Fig. 2.4 Amplitude cross sections of a HG_{00} mode of power 0.9 W, a HG_{10} mode of power 0.1 W, and the sum of both with a total power of 1 W. To first order, the combination of HG_{00} and HG_{10} modes is equivalent to a translated HG_{00} mode

simulation package FINESSE [13], which was used for several simulation tasks described in this thesis.

2.5 The Laguerre-Gauss Mode Sets

The LG modes are solutions to the paraxial wave equation in cylindrical polar coordinates, as opposed to in Cartesian coordinates in the case of HG modes. Unlike the HG modes therefore, the complex amplitude function for LG modes is not separable in x and y, and so LG modes are not eigenmodes of astigmatic optical resonators. LG modes are commonly expressed in two different forms, which I will refer to as the sinusoidal mode set and the helical mode set. While both sets of LG modes have the property of axisymmetry, only the helical set all have circularly symmetric intensity profiles. This property can be useful for reducing the effects of Brownian thermal noise, as is described in further detail later on in Sect. 2.6. Helical LG beams also have the unusual property of carrying orbital angular momentum, which has made them the subject of study by the scientific community in the last two decades or so [1]. This trait has led to their use as ‘optical spanners’ and ‘optical waveguides’ [20] in the bio-photonics and cold atoms fields.

The complex amplitude distribution of the sinusoidal LG mode set is given by

$$u_{p,l}^{\text{cosine}}(r,\phi,z) = \frac{2}{w(z)}\sqrt{\frac{2p!}{\pi(|l|+p)!}}\exp\left(\mathrm{i}\left(2p+|l|+1\right)\Psi(z)\right) \times \left(\frac{\sqrt{2}r}{w(z)}\right)^{|l|} L_p^l\left(\frac{2r^2}{w(z)^2}\right)\exp\left(-\mathrm{i}k\frac{r^2}{2q(z)}\right)\cos(l\phi), \quad (2.14)$$

where all variables are as defined for Eq. 2.11, except p, l and L_p^l, which are the radial mode index, the azimuthal mode index, and the associated Laguerre polynomials respectively. The complex amplitude of helical LG modes shown in Eq. 2.15 is similar in most respects to that for the sinusoidal set, except for the different azimuthal dependence of $\exp(\mathrm{i}l\phi)$ instead of $\cos(l\phi)$. This azimuthal phase dependence is what gives helical LG modes with non-zero l orbital angular momentum. The mode order of both sets of LG beams is given by $2p + l$.

$$u_{p,l}^{\text{helical}}(r,\phi,z) = \frac{1}{w(z)}\sqrt{\frac{2p!}{\pi(|l|+p)!}}\exp\left(\mathrm{i}\left(2p+|l|+1\right)\Psi(z)\right) \times \left(\frac{\sqrt{2}r}{w(z)}\right)^{|l|} L_p^l\left(\frac{2r^2}{w(z)^2}\right)\exp\left(-\mathrm{i}k\frac{r^2}{2q(z)}+\mathrm{i}l\phi\right) \quad (2.15)$$

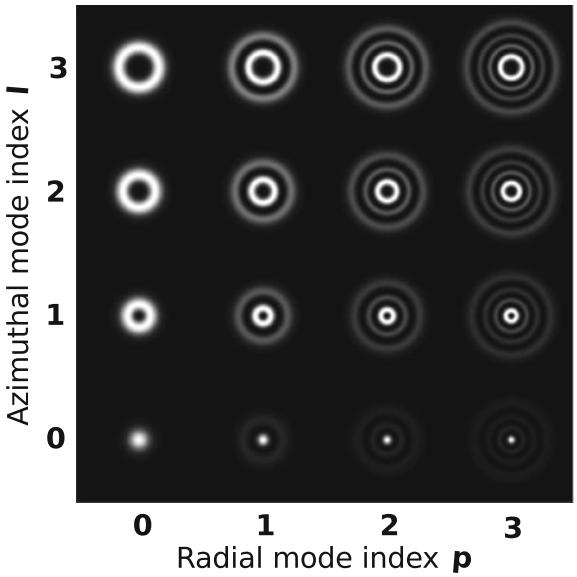

Fig. 2.5 Intensity patterns for helical LG modes up to order 9. The intensity patterns are normalised to have the same peak intensity, for visibility

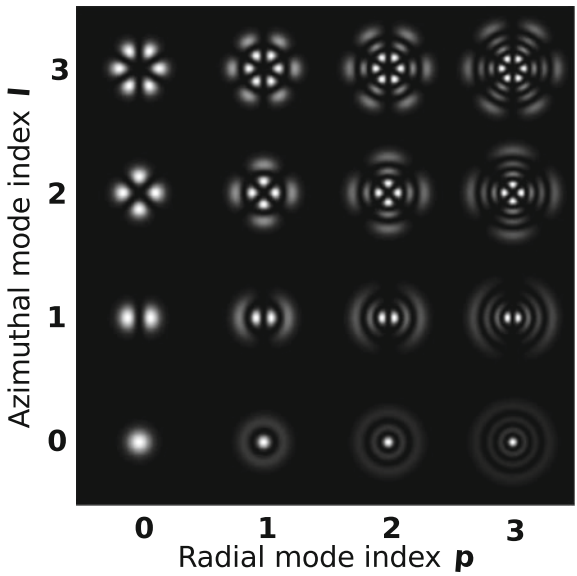

Fig. 2.6 Intensity patterns for sinusoidal LG modes up to order 9. The intensity patterns are normalised to have the same peak intensity, for visibility

The intensity distributions for the modes up to the order 9 of the helical and sinusoidal LG mode sets are shown in Figs. 2.5 and 2.6 respectively. The radial mode index p determines the number of radial nodes that appear in the amplitude cross section of the beam and is equivalent for sinusoidal and helical modes. The azimuthal mode index l determines the number of azimuthal nodes for the cosine modes. For the helical modes however, l determines the number of 2π phase shifts that appear around a circle of constant r and consequently the angular momentum per photon in the beam, which is known to be $l\hbar$ [1]. One may think of the helical LG modes as being a linear combination of two sinusoidal LG modes with the same mode indices but with a phase shift of $\pi/2$ between them, since Euler's theorem states that $\exp(\mathrm{i}l\phi) = \cos(l\phi) + \mathrm{i}\sin(l\phi)$. This fact is useful in understanding the results reported in Sect. 4.4.

As with the HG modes, the LG modes are often observed in optical resonators as the result of imperfect matching of the input beam to the cavity eigenmode. LG modes tend to appear more as the result of axisymmetric mismatches however, such as the mismatch of the input beam waist position or size to that of the cavity eigenmode, rather than misalignments. This coupling can also be seen in the work of Bayer-Helms in [3]. Figure 2.7 illustrates the connection between a mismatch of beam size or position and the effects of adding higher-order LG modes. We see that to a rough approximation, adding a LG_{10} mode to a LG_{00} mode results in another LG_{00} mode but with a different beam size parameter. As in the case of Fig. 2.4, the addition of higher order modes to the sum will increase the accuracy of this approximation.

Since both the LG mode sets and the HG mode sets are complete sets of solutions to the paraxial wave equation, it follows that it is possible to describe any LG mode as a

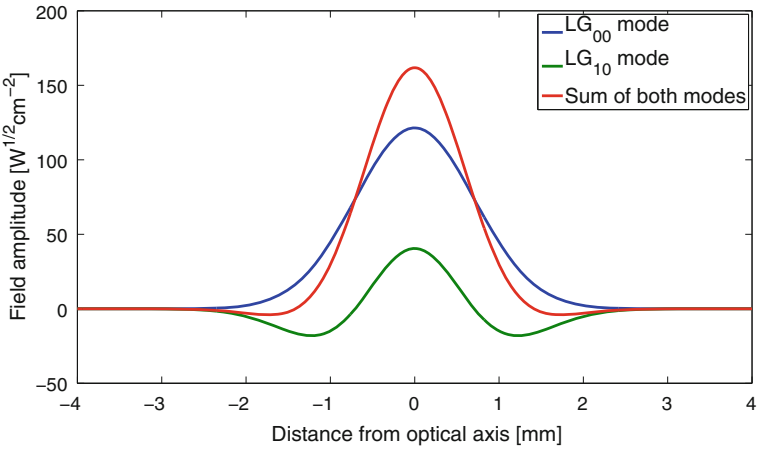

Fig. 2.7 Amplitude cross sections of a LG_{00} mode of power 0.9 W, a LG_{10} mode of power 0.1 W, and sum of both with total power 1 W. To a reasonable approximation, the combination of LG_{00} and LG_{10} modes is equivalent to a LG_{00} mode with a smaller beam spot size parameter

linear combination of HG modes, and vice-versa. We can decompose the LG modes into a weighted sum of HG modes by making use of the relations between Laguerre polynomials and Hermite polynomials, as shown in [4]. The complex amplitude of a LG mode may be given in terms of HG modes by

$$u_{pl}(x, y, z) = \sum_{k=0}^{2p+l} \mathrm{i}^k b(l + p, p, k) u^{\mathrm{HG}}_{2p+l-k,k}(x, y, z), \tag{2.16}$$

where $b(l + p, p, k)$ are the real coefficients given by

$$b(l + p, p, k) = \sqrt{\frac{(2p + l - k)!k!}{2^{(2p+l)}(l + p)!p!}}(-2)^k \mathrm{P}_k^{l+p-k,p-k}(0), \tag{2.17}$$

and $\mathrm{P}_n^{\alpha,\beta}(x)$ are the Jacobi polynomials. This transformation between LG and HG mode sets is used to model LG modes with the simulation software FINESSE, which was designed to use the HG mode set to describe beam shapes. The relation between LG and HG modes demonstrates that it is incorrect to say that HG modes exclusively describe misalignments and translations while LG modes describe exclusively mismatches of beam waist size and position, since both mode sets can describe all four mismatches independently. However, due to the symmetries inherent in the two mode sets, each is a more convenient basis set for describing the mismatches which share their symmetry.

2.6 Reduction in Thermal Noise for Higher-Order LG Beams

The thermal noise equations given in Sect. 2.1 have a dependence on the intensity distribution of the readout beam. This dependence appears in the strain energy factor U in Eq. 2.1 for the case of Brownian noise as

$$U = 2\pi \frac{1-\sigma^2}{Y} \int_0^\infty \tilde{I}(k)^2 dk, \tag{2.18}$$

where σ is the Poisson ratio, Y is the Young's modulus and $\tilde{I}(k)$ is the Hankel transform of $I(r)$, the normalised intensity of the readout beam [31]:

$$\tilde{I}(k) = \int_0^\infty I(r) J_0(kr) r \, dr. \tag{2.19}$$

In the case of a fundamental Gaussian mode readout beam, this gives the results for U shown in Eqs. 2.2 and 2.3, for noise in the substrate and coating respectively. In these equations we see an inverse relationship between U_{sub} and the beam spot size, w, and an inverse square relationship between U_{coat} and w.

The dependence of the Brownian noise on the intensity distribution of the readout beam is best understood in terms of 'averaging' over the fluctuations on the mirror surface. Put simply, the more evenly spread the power in the readout beam is, the better the beam averages over surface distortions, and the less significant the Brownian component of phase noise in the beam becomes. The intensity of fundamental mode beams with very large beam sizes on the mirrors will be very evenly distributed. However, beam sizes on the mirrors cannot be made arbitrarily large due to problems associated with beam clipping losses. This is where so-called flat beams such as mesa-beams and higher-order LG beams have an advantage over the fundamental Gaussian beam, as they can average over the surface better for a given clipping loss.

The clipping loss at an optical component is the fraction of the optical power in the beam that is not incident on the optical surface, i.e. that which is lost beyond its perimeter. This can be calculated as

$$L_{\text{clip}} = 1 - \int_0^{2\pi} d\phi \int_0^R I(r, \phi) r \, dr \, d\phi, \tag{2.20}$$

where $I(r, \phi)$ is the beam intensity distribution function and R is the radius of the optical component. In order to make a fair comparison between the thermal noise performances of different mode shapes we must ensure that all the modes compared have the same clipping losses at a mirror of given size. Since higher-order LG beams are more spatially extended it is therefore necessary to compare beams with different spot sizes.

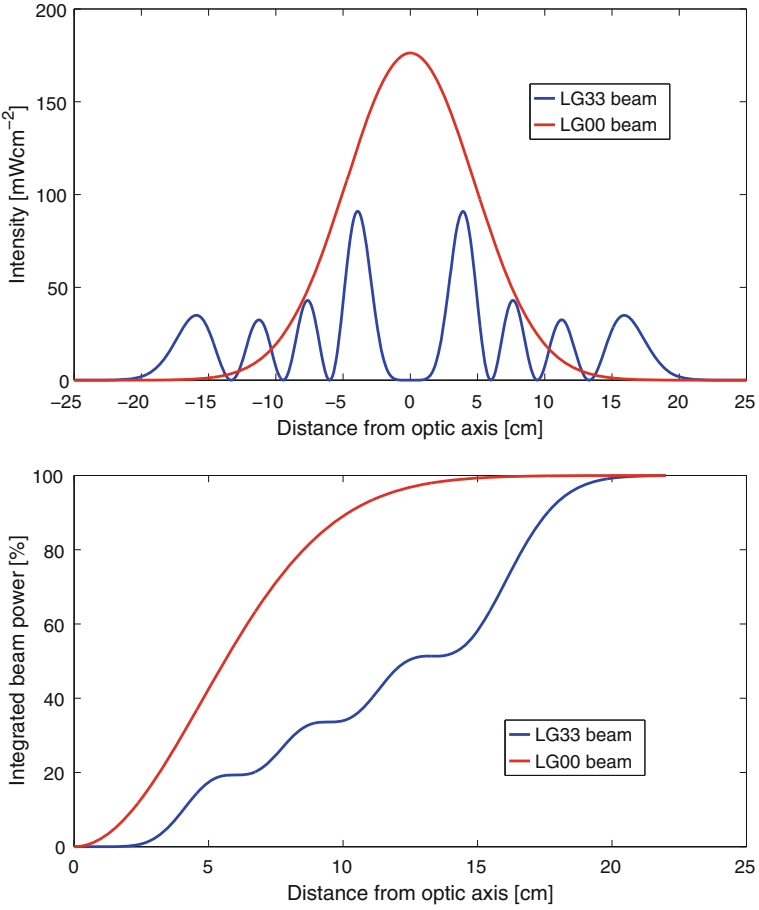

Fig. 2.8 The upper panel shows the intensity as a function of distance from the optic axis for a LG_{33} beam and a LG_{00} beam, both of which experience a 1 ppm clipping loss on a mirror with a radius of 25 cm and have equal total beam powers of 1 W. The lower panel shows the integrated beam power as a function of distance from optic axis for the same two beams

For a given amount of clipping loss on a circular[3] mirror face of a given radius, the optical power is distributed more evenly for higher-order LG beams than for the fundamental LG_{00} beam. This effect is illustrated in Fig. 2.8. The upper panel of Fig. 2.8 is a plot of the intensity profiles of a LG_{33} mode and a LG_{00} mode, both of which have the same total power, and the same clipping loss of 1 ppm on a fixed optic size. It is clear that the peak intensity of the LG_{00} is higher than that of the LG_{33}, indicating that more of the total power is concentrated in one region. The lower

[3] Only cylindrical mirrors are considered in this discussion because this geometry gives the mirror a high Q factor. This reduces the advantage of using higher-order HG modes, which would average better over the surface of rectangular mirrors.

panel shows the integrated beam power as a function of distance from the optical axis, for the same two beams. The average gradient of the slope for the LG_{33} beam is shallower than that of the LG_{00} beam, again demonstrating that the beam power is more evenly spread over the surface of the optic for the LG_{33} beam.

The idea of using different beam shapes to reduce the thermal noise levels in this way originally came from a proposal to use flat top, or 'mesa' beams [8]. However, these beams have the disadvantage of being incompatible with the currently used spherical mirror surfaces. The maturity of the technology to manufacture the 'Mexican hat' mirrors that would be required to support such a beam in a cavity is much less than the technology for manufacturing spherical mirrors. Since higher-order LG modes also offer a thermal noise advantage, but are compatible with the currently used spherical mirrors, we found this idea to be more favourable for consideration in the context of gravitational wave interferometers.

2.7 Coating Brownian Thermal Noise Reduction Factors for Higher-Order Modes

2.7.1 Helical Laguerre-Gauss Modes

After Mours' initial paper suggesting the use of higher-order LG modes as a flat beam candidate for thermal noise reduction [26], Vinet published calculations of the thermal noise performance for mesa-beams and higher-order LG modes in [31], and also for higher-order HG modes in [30]. I will summarise these results here for the coating Brownian noise, as this is currently expected to be the dominant test mass thermal noise source in the second generation of gravitational wave detectors. I will also take the additional step of accounting for the different beam sizes required to maintain a fixed clipping loss of 1 ppm for each mode.

In [31] Vinet calculated the advantage of higher-order beams for coating Brownian noise in the numerical values g_{pl}, which scale the strain energy as

$$U_{pl}^{\text{CoatBrown}} = \delta_C \frac{(1+\sigma)(1-2\sigma)}{2\sqrt{\pi} Y w^2} g_{pl} \tag{2.21}$$

where all other symbols are as defined in Eq. 2.3. Table 2.1 shows some numerical values of g_{pl}.

However, in order to make a fair comparison between the different modes, we should compare beams with the same clipping losses. Table 2.2 shows the beam size scaling factors a_{pl} for LG_{pl} modes relative to the LG_{00} mode in order that each mode has the same clipping loss of 1 ppm on an arbitrary sized mirror.

Since the coating Brownian noise scales with the inverse square of the beam size parameter (see Eqs. 2.3 and 2.21), we must take account of the beam size scaling factors when calculating the real thermal noise improvement of higher-order LG modes. We therefore calculate the actual coating Brownian noise power spectral density improvement factor as

$$\Theta_{pl}^{\text{CoatBrown}} = \frac{a_{pl}^2}{g_{pl}}. \tag{2.22}$$

These coating Brownian noise improvement factors for higher-order LG modes, normalised for 1 ppm clipping loss, are shown in Table 2.3.

In the case of the LG_{33} mode, for which the majority of the research described in thesis was carried out, we see that the coating Brownian noise power spectral density is reduced by a factor of 2.65 from the level experienced when using the LG_{00} mode as the readout beam. It was this clear and significant potential advantage of using the LG_{33} mode that encouraged us to investigate it further within the context of gravitational wave interferometers. The improvement factors offered by LG_{pl} modes for other thermal noise sources are shown in appendix A.

2.7.2 Hermite-Gauss Modes

Although higher-order HG modes might not be expected to give as good thermal noise performance as the higher-order helical LG modes due to their lack of circularly symmetric intensity profiles, it is still interesting to see what improvement they can offer over the LG_{00} mode. This is especially interesting in light of some of the results reported in Chap. 5, where we saw that a 10 m suspended cavity appeared to preferentially resonate with HG modes despite being pumped with a LG mode.

The beam size scaling factors a_{nm} for HG_{nm} modes, relative to the LG_{00} mode, required to give a 1 ppm clipping loss are shown in Table 2.4.

Table 2.1 Coating Brownian noise scaling factors g_{pl} for LG_{pl} modes relative to the LG_{00} mode. The same beam size parameter is assumed for each mode

l p	0	1	2	3	4	5
0	1	0.5	0.34	0.27	0.22	0.19
1	0.5	0.31	0.23	0.19	0.16	0.14
2	0.38	0.25	0.19	0.16	0.14	0.12
3	0.31	0.21	0.17	0.14	0.12	0.11
4	0.27	0.19	0.15	0.13	0.11	0.10
5	0.25	0.17	0.14	0.12	0.11	0.10

Table 2.2 Beam size scaling factors a_{pl} between LG_{00} and LG_{pl} modes that give 1 ppm clipping loss on an arbitrary sized circular mirror [30]

l / p	0	1	2	3	4	5
0	1.00	0.836	0.741	0.675	0.626	0.587
1	0.920	0.785	0.707	0.650	0.606	0.571
2	0.850	0.747	0.679	0.628	0.589	0.556
3	0.804	0.715	0.655	0.609	0.573	0.544
4	0.768	0.689	0.634	0.593	0.559	0.535
5	0.737	0.666	0.616	0.578	0.547	0.529

The results for the coating Brownian noise power spectral density improvement factors $\Theta_{nm}^{\text{CoatBrown}}$ for HG_{nm} modes over the LG_{00} mode were calculated in the same way as for LG modes as

$$\Theta_{nm}^{\text{CoatBrown}} = \frac{a_{nm}^2}{g_{nm}}. \tag{2.23}$$

Table 2.3 Coating Brownian noise power spectral density improvement factors $\Theta_{pl}^{\text{CoatBrown}}$ for LG_{pl} modes over the LG_{00} mode, where all modes are scaled to give 1 ppm clipping loss on a fixed mirror size

l / p	0	1	2	3	4	5
0	1.00	1.40	1.61	1.69	1.78	1.81
1	1.66	1.99	2.17	2.22	2.30	2.33
2	1.90	2.23	2.42	2.47	2.47	2.58
3	2.09	2.44	2.52	2.65	2.74	2.69
4	2.18	2.50	2.68	2.70	2.84	2.86
5	2.17	2.61	2.71	2.78	2.72	2.80

Table 2.4 Beam size scaling factors a_{nm} between HG_{00} and HG_{nm} modes to give 1 ppm clipping loss on an arbitrary sized circular mirror

m / n	0	1	2	3	4	5
0	1	0.910	0.842	0.789	0.746	0.710
1	0.910	0.850	0.798	0.754	0.718	0.686
2	0.842	0.798	0.756	0.721	0.689	0.662
3	0.789	0.754	0.721	0.690	0.664	0.640
4	0.746	0.717	0.690	0.664	0.640	0.619
5	0.710	0.687	0.662	0.640	0.619	0.600

Table 2.5 Coating Brownian noise power spectral density improvement factors $\Theta_{nm}^{\text{CoatBrown}}$ for HG_{nm} modes over the HG_{00} mode, where all modes are scaled to give 1 ppm clipping loss on a fixed mirror size

m n	0	1	2	3	4	5
0	1	1.10	1.11	1.08	1.05	1.02
1	1.10	1.29	1.33	1.40	1.30	1.27
2	1.10	1.33	1.40	1.41	1.41	1.39
3	1.08	1.32	1.41	1.44	1.45	1.45
4	1.05	1.30	1.41	1.45	1.47	1.47
5	1.02	1.27	1.39	1.45	1.47	1.48

The numerical values for these improvement factors are shown in Table 2.5 for HG_{nm} modes up to HG_{55}. From this table we can see that higher-order HG modes do have a coating Brownian noise power spectral density advantage over the HG_{00} mode, though this improvement is less significant than those calculated for the LG modes as shown in Table 2.3. At the equivalent mode order as the LG_{33} mode, the HG_{45} offers only a factor 1.47 improvement, compared with the LG_{33} improvement of 2.65. The improvement factors offered by HG_{nm} modes for other thermal noise sources are shown in appendix A.

2.8 Thermal Lensing

Another thermal effect, aside from thermal noise itself, which must be considered is that of thermal lensing in the optical substrate materials. Light is absorbed in the substrates and coatings of the partially transmissive mirrors; most significantly the power recycling mirror, the arm cavity mirrors and the central beam splitter. For the LG_{00} mode, absorption is strongest in the centre of the mirrors, on the optic axis of the beam. A radial thermal gradient results, and if the thermo-refractive coefficient $\frac{\partial n}{\partial T}$ or the thermal expansion coefficient α of the substrate is non-zero, a thermal lens is produced. An inability to accurately compensate for the thermal lens effect, which will vary with different laser powers and may be non-stationary in time, will lead to imperfect matching of the beam to the interferometer eigenmode and those of the arm cavities therein. This leads to a power loss within the interferometer and an increase in light coupled into higher-order modes [9].

Thermal compensation systems have been in place at the LIGO and Virgo detectors already, but these have proven tricky to implement successfully [23]. With higher laser powers expected in future detectors an advance in the methods of thermal compensation may be required to capitalise on the potential shot noise improvement. Vinet shows in [31] that the higher-order LG modes have a significantly better per-

formance than the LG_{00} mode in terms of thermal distortions of mirrors caused by power absorption in the coating, due to the more even absorption of power across the mirror surface. This is a considerable advantage of higher-order LG beams, as dealing with high-power instabilities such as non-stationary thermal lensing is expected to be one of the major difficulties in commissioning and running the advanced detectors. The use of higher-order LG modes can be expected to relax the requirements on the thermal compensation subsystem.

References

1. L. Allen, M.W. Beijersbergen, R.J.C. Spreeuw, J.P. Woerdman, Orbital angular momentum of light and the transformation of Laguerre-Gaussian laser modes. Phys. Rev. A **45**, 8185–8189 (1992)
2. K. Ballmer S. Gustafson E.K. Hild S. Adhikari, R. Arai, Report of the 3rd generation ligo detector strawman workshop. Technical report LIGO Document T1200031–v3 (2012)
3. F. Bayer-Helms, Coupling coefficients of an incident wave and the modes of spherical optical resonator in the case of mismatching and misalignment. Appl. Opt. **23**, 1369–1380 (1984)
4. M.W. Beijersbergen, L. Allen, H.E.L.O. van der Veen, J.P. Woerdman, Astigmatic laser mode converters and transfer of orbital angular momentum. Opt. Commun. **96**, 123–132 (1993)
5. F. Bondu, P. Hello, J.-Y. Vinet, Thermal noise in mirrors of interferometric gravitational wave antennas. Phys. Lett. A **246**, 227–236 (1998)
6. V.B. Braginsky, S.P. Vyatchanin, Thermodynamical fluctuations in optical mirror coatings. Phys. Lett. A **312**(3–4), 244–255 (2003)
7. H.B. Callen, T.A. Welton, Irreversibility and generalized noise. Phys. Rev. **83**, 34–40 (1951)
8. E. D'Ambrosio, R. O'Shaughnessy, S. Strigin, K.S. Thorne, S. Vyatchanin, *Reducing Thermoelastic Noise in Gravitational-Wave Interferometers by Flattening the Light Beams* (ArXiv General Relativity and Quantum Cosmology e-prints, 2004)
9. J. Degallaix, C. Zhao, L. Ju, D. Blair. Thermal lensing compensation for AIGO high optical power test facility. Class. Quantum Gravity **21**, 903−+ (2004)
10. R.W.P. Drever, Concepts for extending the ultimate sensitivity of interferometric gravitational wave detectors using non-transmissive optics with diffractive or holographic coupling. in *Proceedings of the Seventh Marcel Grossman Meeting on Recent Developments in Theoretical and Experimental General Relativity, Gravitation, and Relativistic Field Theories* (1996), pp. 1401−+
11. M. Evans, S. Ballmer, M. Fejer, P. Fritschel, G. Harry, G. Ogin, Thermo-optic noise in coated mirrors for high-precision optical measurements. Phys. Rev. D (Part. Fields Gravit. Cosmol.) **78**(10), 102003 (2008)
12. A. Freise, K. Strain, Interferometer techniques for gravitational-wave detection. Living Rev. Relativ. **13**(1), 63–91−+ (2010)
13. A. Freise, G. Heinzel, H. Lück, R. Schilling, B. Willke, K. Danzmann, Frequency-domain interferometer simulation with higher-order spatial modes. Class. Quantum Gravity **21**(5), S1067–S1074 (2004)
14. Daniel Friedrich, Bryan W. Barr, Frank Brückner, Stefan Hild, John Nelson, John Macarthur, Michael V. Plissi, Matthew P. Edgar, Sabina H. Huttner, Borja Sorazu, Stefanie Kroker, Michael Britzger, Ernst-Bernhard Kley, Karsten Danzmann, Andreas Tünnermann, Ken A. Strain, Roman Schnabel, Waveguide grating mirror in a fully suspended 10 meter fabry-perot cavity. Opt. Express **19**(16), 14955–14963 (2011)
15. A. Gillespie, F. Raab, Thermally excited vibrations of the mirrors of laser interferometer gravitational-wave detectors. Phys. Rev. D **52**, 577–585 (1995)

16. S. Goßler, A. Bertolini, M. Born, Y. Chen, K. Dahl, D. Gering, C. Gräf, G. Heinzel, S. Hild, F. Kawazoe, O. Kranz, G. Kühn, H. Lück, K. Mossavi, R. Schnabel, K. Somiya, K.A. Strain, J.R. Taylor, A. Wanner, T. Westphal, B. Willke, K. Danzmann. The AEI 10 m prototype interferometer. Class. Quantum Gravity **27**(8), 084023−+ (2010)
17. J. Hallam, S. Chelkowski, A. Freise, S. Hild, B. Barr, K. A. Strain, O. Burmeister, and R. Schnabel. Coupling of lateral grating displacement to the output ports of a diffractive Fabry-Perot cavity. J. Optics A Pure Appl. Opt. **11**(8), 085502−+ (2009)
18. G.M. Harry, The LIGO Scientific Collaboration. Advanced ligo: the next generation of gravitational wave detectors. Class. Quantum Gravity **27**(8), 084006 (2010)
19. G.M. Harry, M.R. Abernathy, A. E. Becerra-Toledo, H. Armandula, E. Black, K. Dooley, M. Eichenfield, C. Nwabugwu, A. Villar, D.R.M. Crooks, G. Cagnoli, J. Hough, C.R. How, I. MacLaren, P. Murray, S. Reid, S. Rowan, P.H. Sneddon, M.M. Fejer, R. Route, S.D. Penn, P. Ganau, J.-M Mackowski, C. Michel, L. Pinard, A. Remillieux, Titania-doped tantala/silica coatings for gravitational-wave detection. Class. Quantum Gravity **24**(2), 405–415 (2007)
20. H. He, M.E.J. Friese, N.R. Heckenberg, H. Rubinsztein-Dunlop, Direct observation of transfer of angular momentum to absorptive particles from a laser beam with a phase singularity. Phys. Rev. Lett. **75**(5), 826–829 (1995)
21. S. Hild, M. Abernathy, F. Acernese, et al., Sensitivity studies for third-generation gravitational wave observatories. Class. Quantum Gravity **28**(9), 094013 (2011)
22. F.Y. Khalili, Reducing the mirrors coating noise in laser gravitational-wave antennae by means of double mirrors. Phys. Lett. A **334**(1), 67–72 (2005)
23. R. Lawrence, M. Zucker, P. Fritschel, P. Marfuta, D. Shoemaker, Adaptive thermal compensation of test masses in advanced LIGO. Class. Quantum Gravity **19**, 1803–1812 (2002)
24. Y. Levin, Internal thermal noise in the LIGO test masses: a direct approach. Phys. Rev. D **57**, 659–663 (1998)
25. Y.T. Liu, K.S. Thorne, Thermoelastic noise and homogeneous thermal noise in finite sized gravitational-wave test masses. Phys. Rev. D **62**(12), 122002 (2000)
26. B. Mours, E. Tournefier, J.-Y. Vinet, Thermal noise reduction in interferometric gravitational wave antennas: using high order TEM modes. Class. Quantum Gravity **23**, 5777–5784 (2006)
27. R. Nawrodt, M.M. Fejer, A. Gretarsson, E. Gustafson, G. Harry, J. Hough1, I. MacLaren, S. Penn, S. Reid, R. Route, S. Rowan, C. Schwarz, P. Seidel, J. Scott, A.L, Woodcraft, I.W. Martin, R. Bassiri, Effect of heat treatment on mechanical dissipation in ta2 o5 coatings. Class. Quantum Gravity **27**, 225020 (2010)
28. S. Rowan, J. Hough, D.R.M. Crooks, Thermal noise and material issues for gravitational wave detectors. Phys. Lett. A 347(1–3), 25–32 (2005) (Einstein Special Issue—Special Issue in celebration of this year's World of Physics and the centenary of Einstein's annus mirabilis)
29. K. Somiya, The KAGRA Collaboration. Detector configuration of KAGRA—the Japanese cryogenic gravitational-wave detector. ArXiv e-prints (2011)
30. Jean-Yves Vinet, Thermal noise in advanced gravitational wave interferometric antennas: a comparison between arbitrary order hermite and laguerre gaussian modes. Phys. Rev. D **82**, 042003 (2010)
31. J.-Y Vinet, On special optical modes and thermal issues in advanced gravitational wave interferometric detectors. Living Rev. Relativ. **12**(5), (2009)
32. K. Yamamoto, T. Uchiyama, S. Miyoki, M. Ohashi, K. Kuroda, H. Ishitsuka, T. Akutsu, S. Telada, T. Tomaru, T. Suzuki, N. Sato, Y. Saito, Y. Higashi, T. Haruyama, A. Yamamoto, T. Shintomi, D. Tatsumi, M. Ando, H. Tagoshi, N. Kanda, N. Awaya, S. Yamagishi, H. Takahashi, A. Araya, A. Takamori, S. Takemoto, T. Higashi, H. Hayakawa, W. Morii, J. Akamatsu. Current status of the clio project. J. Phys. Conf. Ser. **122**, 8 012002 (2008)

http://www.springer.com/978-3-319-01374-9

Precision Interferometry in a New Shape
Higher-order Laguerre-Gauss Modes for Gravitational Wave Detection
Fulda, P.
2014, XXII, 154 p. 61 illus., 44 illus. in color., Hardcover
ISBN: 978-3-319-01374-9